J. Phys.: Condens. Matter **21** (2009) 195406 (9pp) doi:10.1088/0953-8984/21/19/195406

Vibrational, optical and structural studies of an amorphous $Se_{0.90}S_{0.10}$ alloy produced by mechanical alloying

K D Machado[1], D F Sanchez[1], G A Maciel[1], S F Brunatto[2], A S Mangrich[3] and S F Stolf[4]

[1] Departamento de Física, Centro Politécnico, Universidade Federal do Paraná, 81531-990, Curitiba, PR, Brazil
[2] Departamento de Engenharia Mecânica, Centro Politécnico, Universidade Federal do Paraná, 81531-990, Curitiba, PR, Brazil
[3] Departamento de Química, Centro Politécnico, Universidade Federal do Paraná, 81531-990, Curitiba, PR, Brazil
[4] Centro de Engenharia e Ciências Exatas, UNIOESTE, 85903-000, Toledo, PR, Brazil

E-mail: kleber@fisica.ufpr.br (K D Machado)

Received 19 November 2008, in final form 17 March 2009
Published 16 April 2009
Online at stacks.iop.org/JPhysCM/21/195406

Abstract

The local atomic order of an amorphous $Se_{0.90}S_{0.10}$ alloy produced by mechanical alloying was studied by x-ray diffraction and extended x-ray absorption fine structure (EXAFS) data obtained at three temperatures, $T = 300$, 200 and 30 K. From the cumulant analysis of the EXAFS data, structural properties such as average interatomic distances, average coordination numbers, Debye–Waller factors and anharmonicity, given by the third cumulant, were obtained. The results found indicate that there is alloying at an atomic level, and Se–S pairs are more disordered and distorted than Se–Se ones due to the milling process.

(Some figures in this article are in colour only in the electronic version)

1. Introduction

The interest in glasses formed by elements Se, S and Te, that is, chalcogenide glasses, has grown in recent years due to their technological applications in electronic, optoelectronic, optical and memory switching devices. Selenium based chalcogenide alloys have high transparency in the broad, middle and far infrared regions and have strong non-linear properties. Alloys formed by Se and S exhibit an electronic conductivity of p-type semiconductors, and some properties related to these alloys have already been studied. Ward [1] obtained vibrational modes for some crystalline Se–S alloys through Raman spectroscopy. Thermal and electrical properties for amorphous samples were determined in some studies [2–4], and recently Musahwar *et al* [5] measured dielectric and electrical properties for Se_xS_{1-x} glasses ($x = 1, 0.95, 0.90, 0.85, 0.80$), and the optical gaps of Se_xS_{1-x} thin films ($x = 0.9, 0.8, 0.7, 0.6$) were determined by Rafea and Farag [6]. However, concerning structural properties, relatively few investigations have been made on these alloys. Kotkata *et al* [7, 8] obtained x-ray diffraction (XRD) measurements for several amorphous and crystalline Se_xS_{1-x} alloys and present some general results, indicating that amorphous alloys can be prepared in a relatively wide compositional range, from $x = 0.5$ to 1, the density of the alloys decreases as the S content is increased and the average total coordination number for Se atoms ($N_{Se} = N_{Se–Se} + N_{Se–S}$) is 2. The XRD technique was also used by Heiba *et al* [9] to study the crystallization of Se_xS alloys, $x = 20, 30, 40$, and crystallite sizes were determined from a refinement using the program FULLPROOF. A more detailed investigation of amorphous alloys was made by Shama [10], which reports the results obtained from simulations of the first shell of the radial distribution functions (RDF) determined for three amorphous Se_xS alloys, $x = 10, 20, 30$. For these alloys, average coordination numbers and average interatomic distances for Se–Se pairs were given, but the existence of Se–S pairs was not considered. For $Se_{10}S$, the values found were

$N_{Se-Se} = 2.1$ and $r_{Se-Se} = 2.369$ Å. It is interesting to note that all samples cited (except those in [6], which were prepared by thermal evaporation) were prepared by quenching. Fukunaga *et al* [11] used the mechanical alloying (MA) [12] technique to produce amorphous Se_xS_{1-x} alloys, in the compositions $x = 1, 0.90, 0.80, 0.70, 0.60$, which were investigated using neutron diffraction (ND) followed by a RDF analysis. However, results were given only for the composition $Se_{60}S_{40}$, and, in this case, they found $N_{Se-Se} = 1.78 \pm 0.018$ and $r_{Se-Se} = 2.37 \pm 0.002$ Å, and again the possibility of having Se–S pairs was not taken into account. In addition, they assumed that the MA process only mixed Se chains and S rings, and that there is no alloying at the atomic level.

Due to the promising applications of Se–S alloys and the lack of a systematic investigation of their structures, we think that a more detailed structural study should be carried out. Thus, here we have studied the formation of an amorphous $Se_{0.90}S_{0.10}$ by MA and also its structural, vibrational and optical properties, using a combination of conventional XRD, synchrotron XRD, extended x-ray absorption fine structure spectroscopy (EXAFS), Raman spectroscopy (RS), optical absorption spectroscopy (OAS) and reverse Monte Carlo simulations (RMC) [13, 14] of the total structure factor $\mathcal{S}(K)$ obtained from synchrotron XRD measurements. From these techniques, structural information such as average coordination numbers, average interatomic distances, Debye–Waller factors associated with structural and thermal disorders, anharmonicity and Einstein temperatures [20, 21] were obtained. In addition, vibrational modes and also the optical gap of the alloy were determined. The results obtained showed the formation of Se–S pairs, indicating that there is alloying at the atomic level, although the average coordination number concerning this pair is small, and this fact has consequences on the optical properties of the alloy, in particular on its optical gap.

2. Experimental procedures

Amorphous $Se_{0.90}S_{0.10}$ (a-$Se_{0.90}S_{0.10}$) samples were produced by milling Se (Aldrich, purity >99.99%) and S (Vetec, purity >99.5%) crystalline powders in the composition above. The powders were sealed together with 15 steel balls (diameter 10 mm), under argon atmosphere, in a steel vial. The weight ratio of the ball to powder was 9:1. The vial was mounted in a Fritsch Pulverisette 5 planetary ball mill and milled at 350 rpm. In order to keep the vial temperature close to room temperature, the milling was carried out by performing cycles of 20 min of effective milling followed by 20 min of rest. To investigate the formation of the alloy, XRD measurements were taken after 4, 14, 25 and 58 h of milling. They were done in a Shimadzu diffractometer using Cu Kα radiation ($\lambda = 1.5418$ Å) in a θ–2θ scanning mode, using a $\Delta 2\theta$ step of 0.04° and each 2θ point was measured at 2 s (4 h), 10 s (14 and 25 h) and 24 s (58 h) intervals. After 58 h of milling, the XRD pattern was characteristic of amorphous samples, showing large amorphous halos without crystalline peaks.

Micro-Raman measurements were performed with a Renishaw spectrometer coupled to an optical microscope and a cooled CCD detector. The 6238 Å line of a HeNe laser was used as exciting light, always in backscattering geometry. The output power of the laser was kept at about 1–3 mW to avoid overheating the samples. All Raman measurements were performed with the samples at room temperature.

Table 1. Parameters of the acquisition of EXAFS data. They were measured from the energy E_i to E_f in ΔE steps during a time interval Δt.

E_i (eV)	E_f (eV)	ΔE (eV)	Δt (s)
12 558	12 647	1	2
12 647	12 697	0.5	2
12 697	13 097	1	4
13 097	13 396	2	4
13 396	13 698	3	4

EXAFS measurements at the Se K-edge were taken at three temperatures, 30, 200 and 300 K, in the transmission mode at beam line D08B-XAFS2 of the Brazilian Synchrotron Light Laboratory- LNLS (Campinas, Brazil). Three ionization chambers were used as detectors. The a-$Se_{0.90}S_{0.10}$ sample was formed by placing the powder on a porous membrane (Millipore, 0.2 μm pore size) in order to achieve optimal thickness (about 50 μm) and it was placed between the first and second chambers. A crystalline Se foil furnished by LNLS was used as the energy reference and was placed between the second and third chambers. The beam size at the sample was 3 mm × 1 mm. The energy and average current of the storage ring were 1.37 GeV and 190 mA, respectively. EXAFS data were acquired according to table 1.

The raw EXAFS data were analyzed following standard procedures. First the EXAFS spectra were energy calibrated, aligned, and isolated from raw absorbance by performing a background removal using the AUTOBK algorithm of the ATHENA [22] program. Next, structural data were obtained by a multiple data set fit using ARTEMIS [22]. Fourier transforms were performed considering Hanning window functions in the following ranges: 3.7–15.5 $Å^{-1}$ for the photoelectron momentum k and 1.0–2.9 Å for the uncorrected phase radial distance r. Amplitudes and phase shifts relative to the homopolar and heteropolar bonds needed for the fits were obtained from *ab initio* calculations using the spherical waves method [23] and FEFF8.02 software. Each measurement was fitted simultaneously with multiple k weightings of 1–3 in order to reduce correlation between the fitting parameters.

Synchrotron XRD measurements were carried out at the BW5 beamline [24] at HASYLAB. All data were taken at room temperature using a Si(111) monochromator and a Ge solid state detector. The energy of the incident beam was 121.3 keV ($\lambda = 0.102$ Å), and it was calibrated using a LaB_6 standard sample. The uncertainty in the wavelength is less than 0.5%. The cross section of the beam was 1 × 4 mm^2 ($h \times v$). The powder sample was filled into a thin walled (10 μm) quartz capillary with 2 mm diameter. The energy and average current of the storage ring were 4.4 GeV and 110 mA, respectively. Raw intensity was corrected for deadtime, background, polarization, detector solid angle and Compton scattering, as described in [24]. The total structure

factor was computed from the normalized intensity $I(K)$ according to Faber and Ziman [25] (see (1)).

Absorbance measurements were carried out in a Shimadzu UV-2401-PC spectrometer. In these measurements the a-$Se_{0.90}S_{0.10}$ sample was mixed with KBr and pressed in the form of a pellet. KBr was used as a support and reference.

3. Theoretical background

3.1. Structure factors and RMC simulations

According to Faber and Ziman [25], the total structure factor $\mathcal{S}(K)$ is obtained from the scattered intensity per atom $I_a(K)$ through

$$\mathcal{S}(K) = \frac{I_a(K) - \left[\langle f^2(K)\rangle - \langle f(K)\rangle^2\right]}{\langle f(K)\rangle^2}, \tag{1}$$

$$\mathcal{S}(K) = \sum_{i=1}^{n}\sum_{j=1}^{n} w_{ij}(K)\mathcal{S}_{ij}(K), \tag{2}$$

where K is the transferred momentum, $\mathcal{S}_{ij}(K)$ are the partial structure factors and $w_{ij}(K)$ are given by

$$w_{ij}(K) = \frac{c_i c_j f_i(K) f_j(K)}{\langle f(K)\rangle^2}, \tag{3}$$

and

$$\langle f^2(K)\rangle = \sum_i c_i f_i^2(K),$$

$$\langle f(K)\rangle^2 = \left[\sum_i c_i f_i(K)\right]^2.$$

Here, $f_i(K)$ is the atomic scattering factor and c_i is the concentration of atoms of type i. The partial distribution functions $g_{ij}(r)$ are related to $\mathcal{S}_{ij}(K)$ and $\mathcal{S}(K)$ through

$$g_{ij}(r) = \frac{2}{\pi}\int_0^\infty K\left[\mathcal{S}_{ij}(K) - 1\right]\sin(Kr)\,\mathrm{d}K, \tag{4}$$

and, from these functions, interatomic distances and coordination numbers can be determined.

The structure factors defined by (1) can be used in RMC simulations. The algorithm of the standard RMC method is described elsewhere [13, 14] and its application to different materials is reported in the literature [26–30]. The main idea is to minimize the function

$$\psi^2 = \sum_{i=1}^{m}\frac{\left[\mathcal{S}^{\mathrm{RMC}}(K_i) - \mathcal{S}(K_i)\right]^2}{\delta^2} \tag{5}$$

where $\mathcal{S}(K)$ is the experimental total structure factor, $\mathcal{S}^{\mathrm{RMC}}(K)$ is the estimative of $\mathcal{S}(K)$ obtained by RMC simulations, δ is a parameter related to the convergence of the simulations and to the experimental errors, and the sum is over m experimental points. To perform the simulations we have considered the RMC program available on the internet [14] and cubic cells with 5000 and 16 000 atoms. The total structure factor obtained from XRD measurements was used as input data for the simulations.

3.2. EXAFS analyses

In order to obtain structural information from EXAFS measurements, measurements at three temperatures were taken, and a cumulant expansion [15–21] was used. Thus, the Debye–Waller factor (the second cumulant C_2 or the mean square relative displacement—MSRD) for each absorber–scatterer pair was written as the sum of two factors, a static or structural component, σ^2_{st}, which is independent of temperature, and a thermal dependent factor σ^2_T [19–21]. The third cumulant C_3 was also written as a sum of a static or structural term $C_{3,\mathrm{st}}$ and a temperature dependent $C_{3,T}$ factor. The temperature dependent functions use Einstein correlated models, following [19, 20]. The second cumulant C_2 is given by

$$\sigma^2(T) = C_2 = \sigma^2_T + \sigma^2_{\mathrm{st}} = \frac{\hbar^2}{2\mu k_{\mathrm{B}}\Theta_{\mathrm{E}}}\frac{1+z}{1-z} + \sigma^2_{\mathrm{st}} \tag{6}$$

and the third cumulant C_3 is

$$C_3(T) = C_{3,T} + C_{3,\mathrm{st}} = \frac{k_3\hbar^6}{2\mu^3 k_{\mathrm{B}}^4\Theta_{\mathrm{E}}^4}\frac{1+10z+z^2}{(1-z)^2} + C_{3,\mathrm{st}} \tag{7}$$

where $h = 2\pi\hbar$ is Planck's constant, Θ_{E} is the Einstein temperature, $z = \mathrm{e}^{-\Theta_{\mathrm{E}}/T}$, μ is the reduced mass for an absorber–scatterer pair (Se–Se or Se–S), k_{B} is the Boltzmann constant and k_3 is the cubic anharmonicity constant that appears in the one-dimensional effective potential expansion [20]

$$V(r - r_0) = k_{\mathrm{e}}(r - r_0)^2 - k_3(r - r_0)^3 + \cdots \tag{8}$$

and r_0 is the minimum of the effective pair potential, k_{e} is the effective harmonic spring constant given by $k_{\mathrm{e}} = \mu\omega_{\mathrm{E}}^2$, where $\omega_{\mathrm{E}} = k_{\mathrm{B}}\Theta_{\mathrm{E}}/\hbar$ and the Einstein frequency ν_{E} is $\nu_{\mathrm{E}} = \omega_{\mathrm{E}}/2\pi$. It should be noted that the average coordination numbers $N_{\mathrm{Se–Se}}$ and $N_{\mathrm{Se–S}}$ were constrained to be the same at the three temperatures during the fitting.

3.3. Optical band gap determination

A simple and direct way of extracting the optical band gap is to determine the wavelength at which the extrapolations of the baseline and the absorption edge cross [31]. However, by a McLean analysis of the absorption edge more information about the lowest energy interband transition can be obtained. The absorption coefficient γ follows the equation [32]

$$\gamma h\nu = (h\nu - E_{\mathrm{g}})^{\frac{1}{n}} \tag{9}$$

where E_{g} is the band gap and ν is the frequency of the incident beam. The analysis consists of fitting the absorption edge to (9) and determining experimental values for E_{g} and n. $n = 2$ corresponds to a direct allowed transition. $n = \frac{2}{3}$ implies a direct forbidden transition. $n = \frac{1}{2}$ is associated with an indirect allowed transition and $n = \frac{1}{3}$ implies an indirect forbidden transition. The absorbance A, the absorption coefficient γ and the thickness d of a sample are related by $\gamma = A/d$ and, for absorbance measurements on powders, in which the

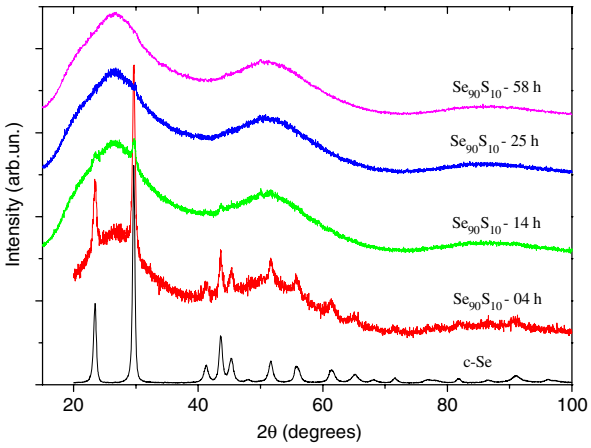

Figure 1. XRD measurements obtained for a-$Se_{0.90}S_{0.10}$ after selected milling times: 4, 14, 25 and 58 h. The XRD pattern for c-Se is also shown for comparison.

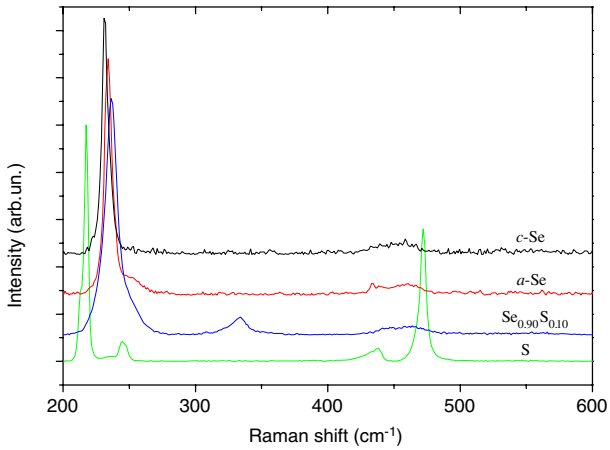

Figure 2. Raman spectra for a-$Se_{0.90}S_{0.10}$, for the starting powders of c-Se (top) and c-S (bottom) and also for a-Se produced by MA.

polycrystalline or amorphous samples are dispersed into a powder support such as KBr, the mixture is pressed in the form of a pellet. In this case, the thickness d and the absorption coefficient γ of the sample become unknown. Thus, (9) must be modified to

$$Ah\nu = C(h\nu - E_g)^{\frac{1}{n}} \tag{10}$$

where C represents the thickness of the sample and is a parameter to be included in the fitting procedure.

4. Results and discussion

4.1. Formation of a-$Se_{0.90}S_{0.10}$

Figure 1 shows the XRD measurements obtained for a-$Se_{0.90}S_{0.10}$ as a function of the milling time. In this figure the XRD pattern for the crystalline selenium powder (c-Se) used as the starting material is also shown for comparison.

After 4 h of milling, the amorphous halos could already be seen, superimposed on the Se crystalline peaks, which almost disappeared at 14 h of milling. Only the most intense crystalline Se peaks remained around 23°, 30° and 44°.

Keeping the milling, at 25 h only a small peak around 30° was seen, indicating that the sample was almost completely amorphous. It is interesting to note that Fukunaga *et al* [11] found that a milling time of 20 h was enough to produce a-$Se_{0.90}S_{0.10}$. We think that the different number of balls used and the different total mass of the starting powder can explain this, since these differences will result in a free volume inside the vial larger for us than for them, and MA is very sensitive to the milling conditions [12]. Finally, after 58 h the crystalline peaks disappeared and an amorphous sample without crystalline peaks of pure Se, S or crystalline Se–S alloy was obtained.

4.2. Raman spectroscopy results

In order to determine the structure of the alloy, the first question to be answered was the existence of Se–S pairs in it. Fukunaga *et al* [11] claimed that MA produces only a mixing of Se chains and S rings, and that there is no alloying at the atomic level. Shama [10] also followed this hypothesis, but for a quenched sample. To investigate this possibility, we made RS measurements on a-$Se_{0.90}S_{0.10}$. Figure 2 shows the results obtained for the alloy, for the c-Se and c-S starting powders and also for an amorphous Se sample (a-Se) obtained by MA, for comparison. The a-Se sample was produced by considering the same milling conditions used to make a-$Se_{0.90}S_{0.10}$.

Table 2. Raman modes obtained from fitting the peaks in figure 2 to Lorentzian functions and their correspondence to modes found in c-Se, a-Se and Se–S alloys.

Mode	Frequency (cm^{-1})	Mode found in	Corresponds to mode (cm^{-1})
A_1, E	236	c-Se and a-Se [36]	235
A_2, E	253	c-Se and a-Se [36]	250
A_1	327	c-$Se_{0.33}S_{0.67}$ [1]	344
A_1	334	c-$Se_{0.33}S_{0.67}$ [1]	360
A_1	356	c-$Se_{0.33}S_{0.67}$ and c-$Se_{0.05}S_{0.95}$ [1]	380
A_1	445	c-$Se_{0.33}S_{0.67}$ and c-$Se_{0.05}S_{0.95}$ [1] and also c-Se and a-Se [36]	435
A_1	463	c-$Se_{0.33}S_{0.67}$ and c-$Se_{0.05}S_{0.95}$ [1] c-Se and a-Se [36]	474

From figure 2 it can be seen that some vibrational modes associated with c-Se have corresponding modes in a-Se and also in a-$Se_{0.90}S_{0.10}$, and they are given in table 2. This was already expected because there is a high quantity of Se in the alloy and this also happened with other Se-based alloys [33–35]. However, a large peak around 334 cm^{-1} appears in the measurement of the alloy, and it cannot be associated with Se–Se vibrations, either in crystalline or amorphous Se, or with S–S vibrations. In addition, Ward [1] obtained RS measurements for $Se_{0.05}S_{0.95}$ and $Se_{0.33}S_{0.67}$ crystalline alloys and found three Se–S modes in the same region where our peak is located, around 344, 360 and 380 cm^{-1}. Thus, the conclusion is that Se–S pairs are found in our alloy, as well as Se–Se and S–S ones. By fitting the Raman peaks using Lorentzian functions we have determined the Raman modes given in table 2.

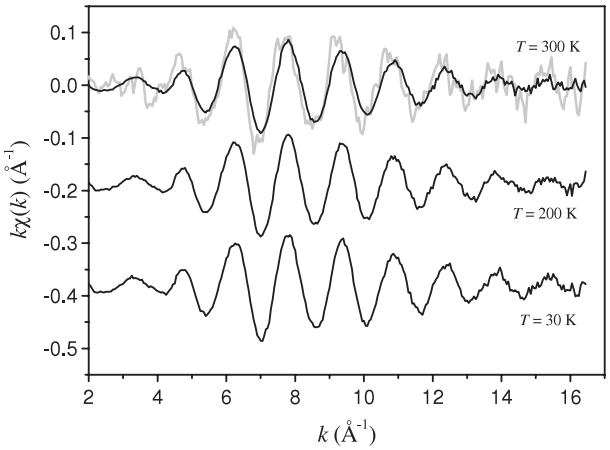

Figure 3. Normalized and k-weighted Se K-edge EXAFS data $k\chi(k)$ for a-$Se_{0.90}S_{0.10}$ at 300 K (top), 200 K (middle) and 30 K (bottom), and also the Se K-edge EXAFS data $k\chi(k)$ for the Se foil used as reference, for comparison (gray).

4.3. EXAFS results

Since we have seen that Se–Se and Se–S pairs can be found in a-$Se_{0.90}S_{0.10}$, we proceeded to the EXAFS analyses at Se K-edge. Figure 3 shows the normalized and k-weighted Se K-edge EXAFS data $k\chi(k)$ for a-$Se_{0.90}S_{0.10}$ at the three temperatures studied, 300 (room temperature), 200 and 30 K, and also the EXAFS data $k\chi(k)$ for the Se foil used as reference (measured at 300 K).

The EXAFS oscillations of a-$Se_{0.90}S_{0.10}$ at three temperatures are very similar, with no differences in phases, but the amplitudes are raised as the temperature is lowered, since the thermal disorder increases with temperature and the oscillations are more damped. Comparing the EXAFS data of the Se foil and a-$Se_{0.90}S_{0.10}$, we see that the Se foil has a more structured spectrum, characteristic of a crystalline sample. In addition, there is a small difference in the frequency of the oscillations, probably due to the Se–S contribution to the EXAFS signal of a-$Se_{0.90}S_{0.10}$. These differences can also be seen if we compare the XANES region and the Fourier transforms of $k\chi(k)$ of the Se foil and a-$Se_{0.90}S_{0.10}$, which is done in figure 4, considering the magnitude and the imaginary part of the Fourier transform.

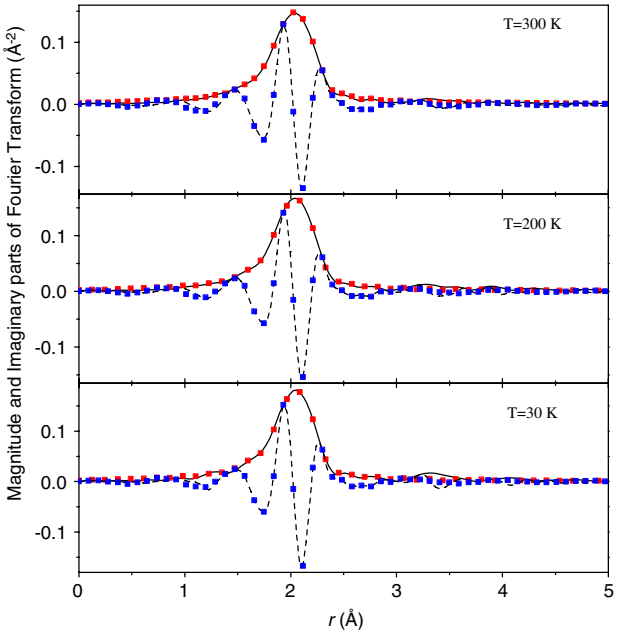

Figure 5. Magnitude (black solid lines) and imaginary parts (black dashed lines) of the non-phase-corrected Fourier transforms of $k\chi(k)$ for 300 K (top), 200 K (middle) and 30 K (bottom) and the simulations obtained in r-space (squares).

To obtain the EXAFS structural data, we made the fitting process both in r-space and in k-space. The magnitude and imaginary part of the Fourier transforms of $k\chi(k)$ are shown in figure 5, together with their simulations in r-space. The structural data obtained are given in tables 3 and 4. As can be seen from the figure, there is a very good agreement between the experimental data and their simulations. It is interesting to note that the maxima of magnitude and imaginary part do not coincide, which is an indication of the asymmetry of the $g(r)$ functions [37].

By Fourier transforming the first shell of the experimental data shown in figure 5 back to k-space we found the EXAFS signals of this shell for each temperature, which are shown in figure 6. Their fits are also shown in this figure, and again the agreement is very good. The structural data obtained are

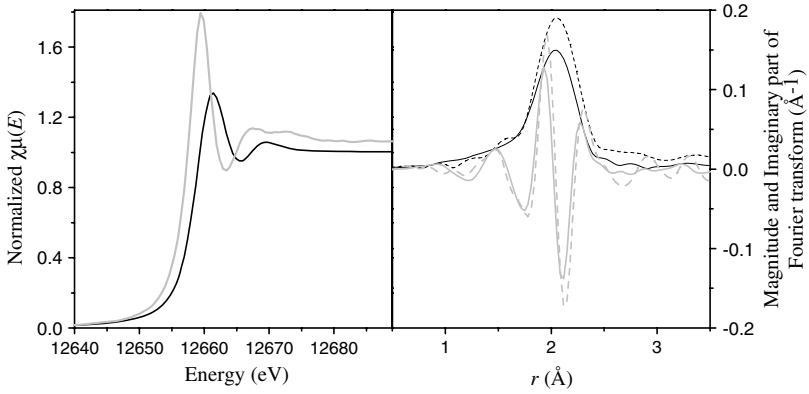

Figure 4. On the left: comparison between the XANES region of a-$Se_{0.90}S_{0.10}$ (black) and of the Se foil used as reference (gray). On the right: magnitude (black lines) and imaginary parts (gray lines) of non-phase-corrected Fourier transform of $k\chi(k)$ of a-$Se_{0.90}S_{0.10}$ (solid lines) and of the Se foil (dashed lines).

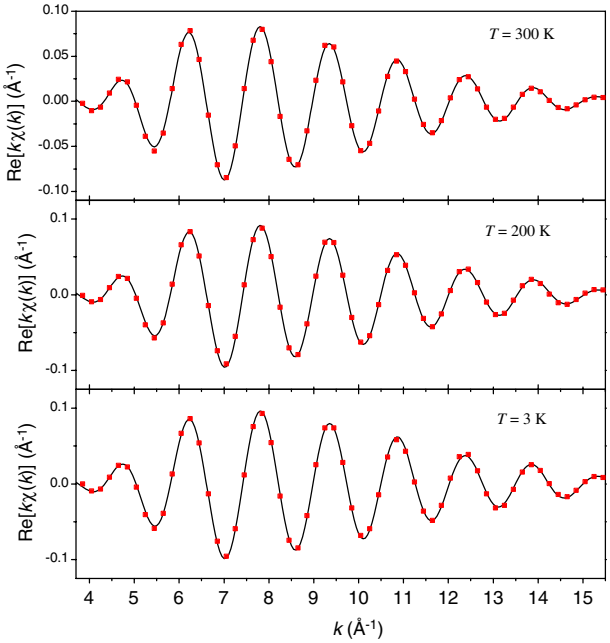

Figure 6. Real part of the Fourier filtered first shell of a-$Se_{0.90}S_{0.10}$ (solid lines) at the three temperatures studied, 300 K (top), 200 K (middle) and 30 K (bottom) and its simulation (squares) at Se K-edge.

Table 3. Einstein temperatures, structural components of C_2 and C_3 cumulants and effective harmonic spring constants obtained from the EXAFS fits shown in figures 5 and 6 for a-$Se_{0.90}S_{0.10}$.

Bond type	Θ_E (K)	σ^2_{st} ($\times 10^{-3}$ Å^2)	$C_{3,st}$ ($\times 10^{-4}$ Å^3)	k_e (eV Å^{-2})
Se–Se	388 ± 11	1.55 ± 0.12	0.00 ± 0.03	10.6
Se–S	411 ± 134	2.55 ± 1.91	-20.0 ± 3.5	6.85

essentially the same as those found in tables 3 and 4. In fact, the fitting process was considered to be finished only when this condition was satisfied.

Some interesting features can be extracted from table 3. The Einstein temperature for Se–Se pairs is smaller than that for Se–S pairs, but due to the different reduced masses, the harmonic spring constant k_e for Se–Se pairs is larger than that for Se–S pairs, indicating that Se–Se bonds are stronger than Se–S ones. The static or structural component of the Debye–Waller factors, σ^2_{st}, is not negligible for both bonds, a result expected due to the amorphous nature of the sample. In addition, the structural part of the third cumulant, $C_{3,st}$, is very large for Se–S bonds, indicating a large anharmonicity associated with these bonds when compared to that found in Se–Se bonds. It is interesting to note from tables 3 and 4 that the main contribution for C_3^{Se-S} is due to the structural part, the thermal contribution being small (see (7)). On the other hand, for Se–Se pairs, the opposite happens, the structural contribution $C_{3,st}$ is null (or very small, considering the error bars), and C_3^{Se-Se} is given by the thermal contribution to the anharmonicity. Concerning the thermal contribution to the Debye–Waller factors (see (6)), even at 30 K it is as important as the structural contribution, and it increases for both

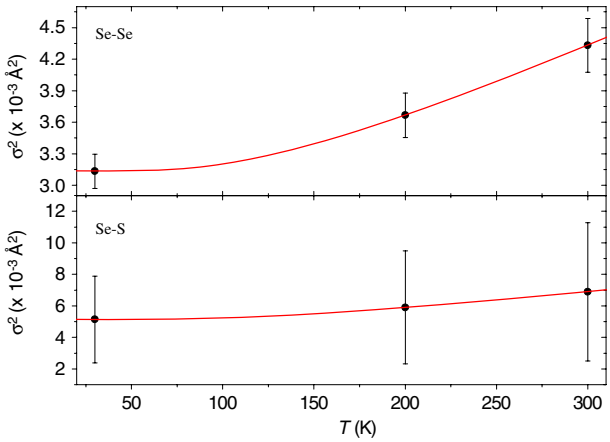

Figure 7. Debye–Waller factors obtained from the fitting process for a-$Se_{0.90}S_{0.10}$ at the three temperatures studied and their simulations considering the correlated Einstein model given by (6).

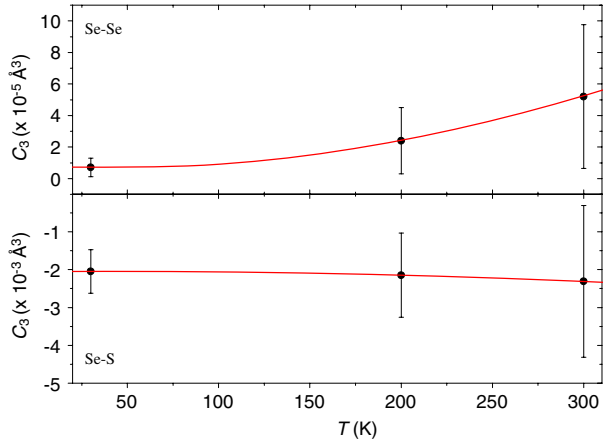

Figure 8. Third cumulants C_3 obtained from the fitting process for a-$Se_{0.90}S_{0.10}$ at the three temperatures studied and their simulations considering the correlated Einstein model given by (7).

Se–Se and Se–S pairs as the temperature rises, as expected. Figures 7 and 8 show the σ^2 and C_3 obtained and the fits from considering (6) and (7).

The average interatomic distance for Se–Se pairs shows a monotonic behavior with temperature, and Se–Se bonds expand as the temperature is raised. The behavior of Se–S bonds with temperature is less clear, since the error bars are larger in this case, probably due to the relatively small quantity of sulfur in the alloy. Figure 9 shows the average interatomic distances for Se–Se and Se–S pairs.

To describe their behavior as a function of T/Θ_E, we considered an exponential function of the form

$$r_{Se-Se}(T) = a + b \exp\left(c\frac{T}{\Theta_E}\right) \qquad (11)$$

and we found $a = 2.345$ Å, $b = 6.1 \times 10^{-4}$ Å and $c = 2.898$. To Se–S pairs, we supposed a parabolic fit given by

$$r_{Se-S}(T) = A + B\left(\frac{T}{\Theta_E}\right) + C\left(\frac{T}{\Theta_E}\right)^2 \qquad (12)$$

Table 4. Structural parameters obtained for a-$Se_{0.90}S_{0.10}$ from the EXAFS analyses.

Bond type	$\langle N\rangle$	$\langle r\rangle$ (Å)	σ^2 ($\times 10^{-3}$ Å^2)	C_3 ($\times 10^{-4}$ Å^3)
		$T = 300$ K		
Se–Se	1.71 ± 0.03	2.350 ± 0.004	4.33 ± 0.26	0.52 ± 0.46
Se–S	0.23 ± 0.04	2.33 ± 0.02	6.90 ± 4.40	-23.1 ± 20.0
		$T = 200$ K		
Se–Se	1.71 ± 0.03	2.347 ± 0.003	3.67 ± 0.21	0.24 ± 0.21
Se–S	0.23 ± 0.04	2.35 ± 0.01	5.90 ± 3.59	-21.5 ± 11.1
		$T = 30$ K		
Se–Se	1.71 ± 0.03	2.346 ± 0.002	3.13 ± 0.16	0.07 ± 0.06
Se–S	0.23 ± 0.04	2.35 ± 0.02	5.14 ± 2.75	-20.5 ± 5.8

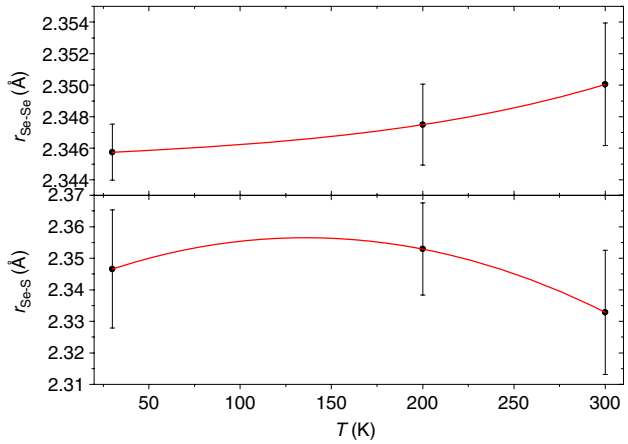

Figure 9. Average interatomic distances r_{Se-Se} and r_{Se-S} obtained from EXAFS for a-$Se_{0.90}S_{0.10}$ and their fits considering (11) and (12).

which furnishes the values $A = 2.34$ Å, $B = 0.099$ Å and $C = -0.15$ Å. From these results, we can determine the thermal expansion coefficient α given by

$$\alpha = \frac{1}{r}\frac{\mathrm{d}r}{\mathrm{d}T}.$$

Using (11), we found

$$\alpha_{Se-Se}(T) = \frac{\frac{c}{\Theta_E}}{1 + \frac{a}{b}\exp\left(-c\frac{T}{\Theta_E}\right)} \qquad (13)$$

and, from (12),

$$\alpha_{Se-S}(T) = \frac{1}{\Theta_E}\frac{B + 2C\left(\frac{T}{\Theta_E}\right)}{A + B\left(\frac{T}{\Theta_E}\right) + C\left(\frac{T}{\Theta_E}\right)^2}. \qquad (14)$$

From (13) and (14), the values for the thermal expansion coefficient at the temperatures studied can be calculated, and are given in table 5. However, the errors associated with $\alpha_{Se-S}(T)$ are large at 200 and 300 K. Then, it is not possible to clearly establish the behavior of $\alpha_{Se-S}(T)$ with temperature.

Comparing our results with those given in [10] for $Se_{10}S$, which is a composition close to ours, it was noted that in that study the average number of Se–Se pairs is $N_{Se-Se} = 2.1$, located at $r_{Se-Se} = 2.369$ Å. In a-$Se_{0.90}S_{0.10}$, the total coordination number of Se is almost 2.0, and there are Se–Se and Se–S pairs, which are located around 2.35 Å. Comparing our data with those obtained by Fukunaga *et al* [11], there is an important difference, since there are Se–S pairs in our alloy, which were not considered by them.

Table 5. Thermal expansion coefficient α for Se–Se and Se–S pairs in a-$Se_{0.90}S_{0.10}$ from the EXAFS analyses using (13) and (14).

Bond type	$\alpha(300)$ (K^{-1})	$\alpha(200)$ (K^{-1})	$\alpha(30)$ (K^{-1})
Se–Se	$(18 \pm 2) \times 10^{-6}$	$(8.6 \pm 0.6) \times 10^{-6}$	$(2.43 \pm 0.08) \times 10^{-6}$
Se–S	$(-1 \pm 1) \times 10^{-4}$	$(-5 \pm 7) \times 10^{-5}$	$(8 \pm 2) \times 10^{-5}$

4.4. RMC simulations

To obtain an independent confirmation of the structural data extracted from EXAFS and also to get some information about S–S pairs, we made RMC simulations [13, 14] of the total structure factor $\mathcal{S}(K)$ obtained from XRD measurements through (1). Here, it is interesting to note that the main contribution to the total structure factor $\mathcal{S}(K)$ is due to the Se–Se pairs. For instance, at $K = 1$ Å^{-1}, the coefficients $w_{ij}(K)$, given by (3), are $w_{Se-Se} = 0.905$, $w_{Se-S} = 0.093$ and $w_{S-S} = 0.002$. Thus, the contribution of $\mathcal{S}_{Se-Se}(K)$ to $\mathcal{S}(K)$ is about 90.5% (see (2)), while the contribution of $\mathcal{S}_{Se-S}(K)$ is around 9.3%, and the remaining 0.2% is associated to $\mathcal{S}_{S-S}(K)$. This fact makes the error bars of the structural parameters related to Se–Se pairs much smaller than those associated with Se–S pairs and, concerning S–S pairs, we have just estimates.

The first point is to determine the density of the alloy. To do this, we used the procedure suggested in [38], and made several simulations for different values of the density ρ keeping minimum distances and δ fixed (see (5)). Thus, we chose the density that minimized the ψ^2_{eq} parameter, which was $\rho = 0.030$ atm Å^{-3}. Then, we made several simulations changing the minimum distances between atoms, in order to find the best values for these parameters. All the simulations

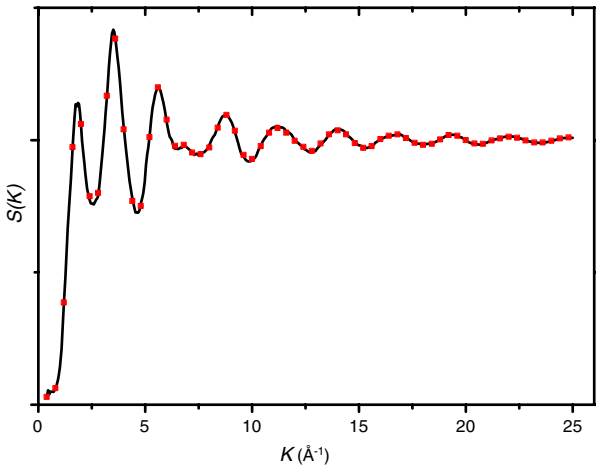

Figure 10. Experimental (full black line) and simulated (red squares) total structure factor for a-$Se_{0.90}S_{0.10}$.

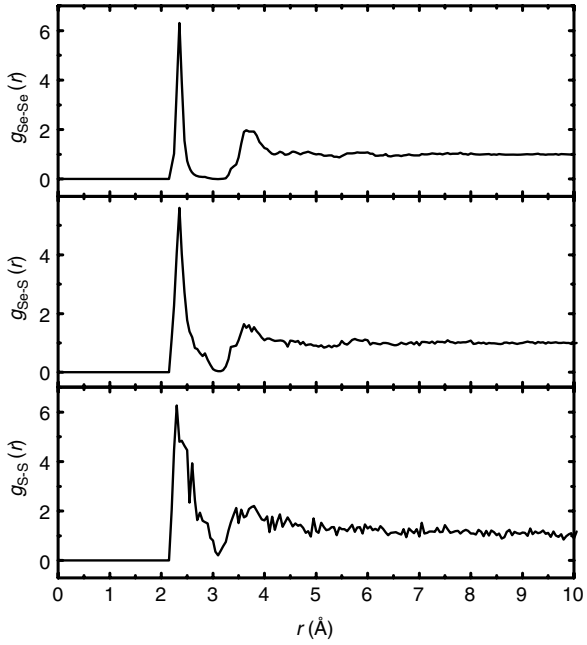

Figure 11. $g_{Se-Se}(r)$, $g_{Se-S}(r)$ and $g_{S-S}(r)$ functions obtained from the RMC simulations for a-$Se_{0.90}S_{0.10}$.

performed followed the procedure below

(i) First, hard sphere simulations without experimental data were made to avoid possible memory effects of the initial configurations in the results. These simulations were run until they reached at least 3×10^6 accepted moves.

(ii) Next, simulations using experimental data were performed, and after reaching convergence the statistically independent configurations were collected, considering at least 1×10^5 accepted movements between one configuration and the next. At the end of the simulations, about 20% of the generated movements were accepted.

The best value obtained for the minimum distance was $r_{min} = 2.20$ Å for all pairs (Se–Se, Se–S and S–S). Taking into account only the experimental total structure factor $\mathcal{S}(K)$, its RMC simulation obtained considering these values, 16 000 atoms and the density found is shown in figure 10. As can be seen, a very good agreement between them is reached.

From the simulations, the partial distribution functions $g_{ij}(r)$ can be obtained and, from them, average coordination numbers and average interatomic distances can be determined. Figure 11 shows the $g_{ij}(r)$ functions obtained from the RMC simulations, and table 6 lists the corresponding structural parameters.

It is interesting to note that the structural data obtained from the RMC simulations (table 6) agree very well with those found from EXAFS analyses (table 4). They were obtained by different techniques and both indicate the existence of Se–S pairs in a-$Se_{0.90}S_{0.10}$.

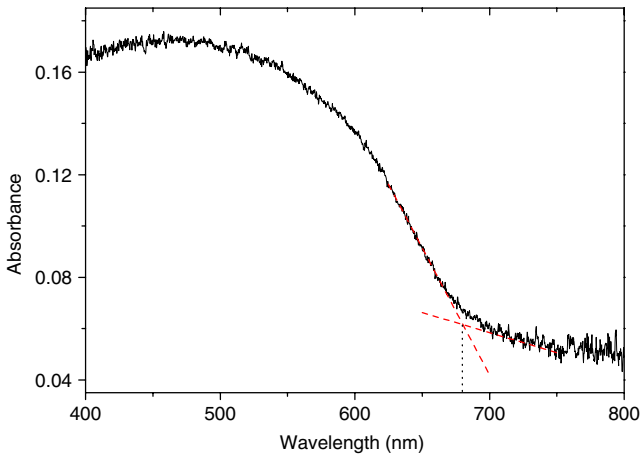

Figure 12. Absorption spectrum determined for a-$Se_{0.90}S_{0.10}$ and extrapolations to the baseline and to the absorption edge (dashed lines). The vertical dotted line indicates the crossing of both lines, which is the estimate of the band gap.

Table 6. Structural parameters obtained for a-$Se_{0.90}S_{0.10}$ from RMC simulations.

Bond type	Se–Se	Se–S	S–S
$\langle N \rangle$	1.8 ± 0.1	0.30 ± 0.15	$\leqslant 0.6$
$\langle r \rangle$ (Å)	2.35 ± 0.06	2.34 ± 0.09	2.30 ± 0.20

4.5. Optical band gap determination

After studying the structural and vibrational properties of a-$Se_{0.90}S_{0.10}$, we determined its optical band gap. Figure 12 shows the absorbance obtained for our alloy. The absorption edge appears around 620–680 nm, and we determined the optical gap using two ways. First, we considered the extrapolations of the baseline and the absorption edge [31], which are shown in figure 12 (dashed lines). This procedure furnished a gap located at 679.7 nm, indicated in the figure by the vertical dotted line, corresponding to the value $E_g = 1.83$ eV.

Next, we fitted the absorption edge region using the McLean procedure [32]. Figure 13 shows the best fit achieved using (10). We found a direct band gap ($n = 2$) at

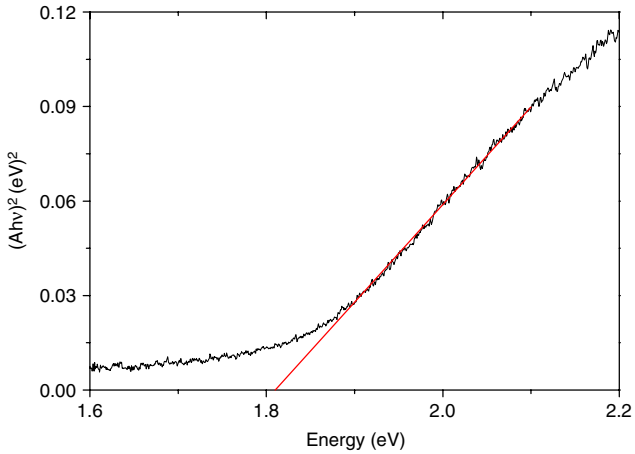

Figure 13. Plot of $(Ah\nu)^2 \times h\nu$ and linear fit for a-$Se_{0.90}S_{0.10}$ to obtain the optical band gap.

$E_g = 1.81$ eV for a-$Se_{0.90}S_{0.10}$. For a comparison, the value found by Rafea and Farag [6] for an amorphous $Se_{0.90}S_{0.10}$ thin film was $E_g = 1.92$ eV.

5. Conclusion

The amorphous $Se_{0.90}S_{0.10}$ alloy was prepared by MA and its local atomic structure investigated. The main conclusions of this study are:

(i) Although in a small quantity, Se–S pairs exist in the alloy, as confirmed by the Raman spectroscopy (see figure 2), indicating that alloying occurs in an atomic level. This is a result that disagrees with the statement made by Fukunaga *et al* [11] that instead of alloying there is only a mixing of Se chains and S rings.

(ii) There is a relevant anharmonicity associated with Se–S pairs, and its origin is associated with the structure of the alloy. The thermal contribution to it, as measured by the third cumulant $C_{3,T}$, is small when compared to the structural term. For Se–Se pairs the anharmonicity is very low and due only to the thermal contribution.

(iii) The optical gap of the alloy corresponds to a direct transition, and the addition of sulfur, even in a small quantity, increases the value of the gap when compared to pure Se.

Acknowledgments

We thank the Brazilian agencies CNPq and CAPES for financial support. This study was also partially supported by LNLS (proposal no. 7093/08). We would like to thank Dr Pál Jóvári for the synchrotron XRD measurements and suggestions about the manuscript.

References

[1] Ward A T 1968 *J. Phys. Chem.* **72** 4133
[2] Kotkata M F, Ayad F M and El-Mously M K 1979 *J. Non-Cryst. Solids* **33** 13
[3] Kotkata M F, El-Fouly M F, El-Behay A Z and El-Wahab L A 1983 *Mater. Sci. Eng.* **60** 163
[4] Mahmoud E A 1990 *J. Therm. Anal.* **36** 1481
[5] Musahwar N, Khan M A M, Husain M and Zulfequar M 2007 *Physica* B **396** 81
[6] Rafea M A and Farag A A M 2008 *Chalc. Lett.* **5** 27
[7] Kotkata M F, Nouh S A, Farkas L and Radwan M M 1992 *J. Mater. Sci.* **27** 1785
[8] Kotkata M F, Füstoss-Wegner M, Toth L, Zental G and Nouh S A 1993 *J. Phys. D: Appl. Phys.* **26** 456
[9] Heiba A K, El-Den M B and El-Sayed K 2002 *Powder Diffract.* **17** 1861
[10] Shama A A 2005 *Egypt. J. Solids* **28** 25
[11] Fukunaga T, Kajikawa S, Hokari Y and Mizutani U 1998 *J. Non-Cryst. Solids* **232–234** 465
[12] Suryanarayana C 2001 *Prog. Mater. Sci.* **46** 1
[13] McGreevy R L 2001 *J. Phys.: Condens. Matter* **13** 877
[14] Gereben O, Jóvári P, Temleitner L and Pusztai L 2007 *J. Optoelectron. Adv. Mater.* **9** 3021
[15] Beccara S A, Dalba G, Fornasini P, Grisenti R, Sanson A and Rocca R 2002 *Phys. Rev. Lett.* **89** 025503
[16] Dalba G, Fornasini P, Grisenti R and Purans J 1999 *Phys. Rev. Lett.* **82** 4240
[17] Dalba G, Fornasini P, Grazioli M and Rocca F 1995 *Phys. Rev.* B **52** 11034
[18] Dalba G, Fornasini P, Gotter R and Rocca F 1995 *Phys. Rev.* B **52** 149
[19] Dalba G, Fornasini P and Rocca F 1993 *Phys. Rev.* B **47** 8502
[20] Frenkel A I and Rehr J J 1993 *Phys. Rev.* B **48** 585
[21] Tröger L, Yokoyama T, Arvanitis D, Lederer T, Tischer M and Baberschke K 1994 *Phys. Rev.* B **49** 888
[22] Ravel B and Newville M 2005 *J. Synchrotron Radiat.* **12** 537
[23] Rehr J J 1991 *J. Am. Chem. Soc.* **113** 5135
[24] Poulsen H F, Neuefeind J, Neumann H B, Schneider J R and Zeidler M D 1995 *J. Non-Cryst. Solids* **188** 63
[25] Faber T E and Ziman J M 1965 *Phil. Mag.* **11** 153
[26] Machado K D, Jóvári P, de Lima J C, Gasperini A A M, Souza S M, Maurmann C E, Delaplane R G and Wannberg A 2005 *J. Phys.: Condens. Matter* **17** 1703
[27] Jóvári P, Kaban I, Steiner J, Beuneu B, Schöps A and Webb M A 2008 *Phys. Rev.* B **77** 035202
[28] Jóvári P, Delaplane R G and Pusztai L 2003 *Phys. Rev.* B **67** 172201
[29] Tengroth C, Swenson J, Isopo A and Borjesson L 2001 *Phys. Rev.* B **64** 224207
[30] Iparraguirre E W, Sietsma J and Thijsse B J 1993 *J. Non-Cryst. Solids* **156–158** 969
[31] Boldish S I and White W B 1998 *Am. Mineral.* **83** 865
[32] McLean T P 1960 *Prog. Semicond.* **5** 55
[33] Machado K D, de Lima J C, Campos C E M, Gasperini A A M, Souza S M, Maurmann C E, Grandi T A and Pizani P S 2005 *Solid State Commun.* **133** 411
[34] Campos C E M, de Lima J C, Grandi T A, Machado K D and Pizani P S 2003 *Solid State Commun.* **126** 611
[35] Sugai S 1987 *Phys. Rev.* B **35** 1345
[36] Guo F Q and Lu K 1998 *Phys. Rev.* B **57** 10414
[37] Cozier E D, Rehr J J and Ingalls R 1988 *X-Ray Absorption* ed D C Koningsberger and R Prins (New York: Wiley)
[38] Gereben O and Pusztai L 1994 *Phys. Rev.* B **50** 14136